Effect of Texture on Strain Localization and Crack Initiation in Polycrystalline Beryllium Under Static Tension: Experimental Study and Micromechanical Simulations

V. MISHIN, I. SHISHOV, E. UBYIVOVK, I. KASATKIN, and A. SHAMSHURIN

The mechanisms of deformation and crack initiation in polycrystalline beryllium during static tension were studied in this work using EBSD analysis and crystal plasticity simulations. Results showed that cold deformation of beryllium was accompanied by an extremely inhomogeneous distribution of accumulated strain associated with different activities of slip systems and grain interactions. The fracture of beryllium occurs by two mechanisms strongly related to its crystallographic texture. Impossibility of slip along the basal and prismatic systems leads to brittle transgranular fracture at small strains. Localization of strain at the conjugation of grains with favorable and unfavorable conditions for prismatic slip produces intergranular cracks due to the exhaustion of beryllium plasticity. Moreover, activation of basal or prismatic slip is not only controlled by the grain orientation but also by the stress concentration raised by grain interactions. The modified Cockcroft–Latham criterion and the stress triaxiality parameter showed a reasonable agreement between the predicted and observed regions of intergranular crack formation. For accurate estimation of the fracture probability, the strong dependence of fracture strain or of the criterion limiting value on the grain orientation should be taken into consideration.

I. INTRODUCTION

BERYLLIUM is an attractive material for aerospace,[1,2] nuclear,[3–6] optical,[7,8] and X-ray [9–11] applications due to a unique combination of its mechanical and physical properties. Improved strength and ductility are crucial for its utilization since the mechanical properties directly affect the reliability and operational time of devices.

Like many other metals with a hexagonal close-packed (hcp) lattice, beryllium forms sharp textures during plastic deformation,[12–15] which cause significant anisotropy of its mechanical properties.[16,17]

The deformation modes for a single crystal of beryllium at room temperature are well known.[18–22] Basal slip on the $\{0001\}$ $\langle 11\text{–}20 \rangle$ system is the main deformation mechanism. Slips on the prismatic $\{10\text{–}10\}$ $\langle 11\text{–}20 \rangle$ and the pyramidal $\langle c + a \rangle$ systems are also possible, but the values of critical resolved shear stresses at room temperature are much higher for these systems. Another deformation mode is the twinning by the $\{10\text{–}12\}$ $\langle 10\text{–}11 \rangle$ system. However, it can only be activated on compression or tension in the directions transverse or parallel to the c-axis of the basal pole, respectively. Meanwhile, deformation of polycrystalline beryllium is much more complex, and it strongly depends on crystallographic texture and the loading path.[12] Each grain in a polycrystalline material is deformed in close interaction with neighboring grains which produces significant local stresses and affects the activation of nonbasal slip systems.[23,24]. The macroscopic behavior of polycrystalline beryllium under various loading conditions has been studied in detail using elastoplastic self-consistent (EPSC) and viscoplastic self-consistent (VPSC) models.[12,13,25–27] In our previous works[15,17], electron backscatter diffraction (EBSD), X-ray diffraction, tensile tests, and numerical simulations with the VPSC model have shown that the formation of a favorable structure and

V. MISHIN, I. SHISHOV, and A. SHAMSHURIN are with the Peter the Great St. Petersburg Polytechnic University, 29 Polytechnicheskaya, St. Petersburg, Russia, 195251. Contact e-mail: shishov_i@list.ru E. UBYIVOVK is with the Saint Petersburg State University, 7-9 Universitetskaya Nab., St. Petersburg, Russia, 199034 and also with the Alferov University, 8/3 Khlopina, St. Petersburg, Russia, 194021. I. KASATKIN is with the Saint Petersburg State University.

texture could be an effective way to improve the mechanical properties of beryllium due to activation of prismatic slip along the {10–10} ⟨11–20⟩ SS. However, the EPSC and VPSC models oversimplify the grain interactions in a polycrystalline material. Thus, it was impossible to evaluate the stress and strain localizations associated with these interactions. At the same time, it is well known that deformation of a polycrystalline material can be accompanied by a significant inhomogeneity of the accumulated plastic strain,[28,29] which can directly affect the material hardening behavior and failure.[30,31]

Beryllium is traditionally considered a brittle material,[32,33] so understanding the relationships between the textures and fracture mechanisms can be critically important for its application. It is well known that the mechanism of fracture (brittle or ductile) and fracture toughness depends on the predominant crystallite orientation since the anisotropy of mechanical properties affects the level of stresses during crack formation and growth.[34] A favorable crystallographic texture of the material increases the resistance to fracture and minimizes the growth of defects during fatigue cycling, which improves the fatigue characteristics of the material.[35] This effect has been reported for steels, zirconium, and titanium alloys.[36–39]

Brittleness of beryllium depends strongly on the predominant crystallographic orientation. Hot-pressed beryllium with random texture is characterized by only 2–3 pct relative elongation, while an extruded rod demonstrates the elongation of 15–20 pct in the extrusion direction.[40] When all other essential parameters, such as grain size and chemical purity, are the same, the effect can be explained by different activities of slip systems (SS). After extrusion, beryllium has a crystallographic texture favorable for the activation of prismatic SS when loading in the extrusion direction, which results in a significant increase in ductility. The grain size and preferred orientation affect the ductile–brittle transition, as it was also theoretically predicted by Armstrong [41].

Wittenauer et al.[42] investigated the plastic properties of polycrystalline hot-rolled beryllium foils during bending. The enhanced ductility resulted from the formation of a coarse-grained structure while the texture had a little effect on the formability. This result has been explained by the fact that the large grains span the entire foil thickness without a need to accommodate the plastic slip at the neighboring grain boundaries. Thus, it is obvious that grain interactions play an important role in beryllium fracture.

This work is focused on the detailed study of deformation and fracture of polycrystalline beryllium during static tension using EBSD analysis in combination with numerical simulations. The main aim is to reveal the relationship between the crystallographic texture of beryllium and the conditions of crack initiation considering the strain localization and grain interactions.

II. MATERIALS AND METHODS

A. Tension Testing and EBSD Analysis

Samples for tension were obtained in two stages. At the first stage, distilled hot-extruded beryllium (99.87 wt pct, excluding BeO) with an initial thickness of 3 mm has been subjected to multipass hot cross rolling in the protective container down to the thickness of 150 μm at 870 °C with intermediate reheating between the passes.[17] Then, the samples were cold rolled at the laboratory mill down to the final thickness of 25 μm in the direction transverse to the direction of hot rolling. After cold rolling, the total logarithmic strain in the normal direction was ε_{ND} = 1.8. The cold rolling procedure was split into several stages. The values of ε_{ND} = 0.2–0.3 were achieved at every stage after which beryllium was subjected to intermediate annealing. A final annealing has also been performed at the end of the cold rolling route prior to further investigations. The intermediate and final annealings were carried out at a temperature of 850 °C for 20 minutes under high vacuum conditions (pressure 5×10^{-7} mbar).

By controlling the rolling route, a required texture can be obtained.[15] A fiber texture [Figure. 1(a)] was formed in the rolled foil to ensure the maximum ductility of beryllium in the tension direction.[17] In addition, cold rolling combined with annealings led to the formation of relatively fine grains in the beryllium structure. The average equivalent spherical diameter of the grains was 11.6 μm [Figure 1(b)].

A special specimen shape (Figure 2) with two parallel stiffening ribs was used in tension tests to ensure strain localization in the working area and to avoid premature fracture of beryllium.

The tests were made at room temperature with a tension speed of 1 μm/s. The motion of the specimen grip was controlled using a Gatan Accutroller Model 902 equipped with a displacement measurement sensor. The loading process was monitored with an optical microscope Olympus BX51 at a magnification of 100X. Tension was stopped after the macrocracks have appeared. The stress–strain curve was not recorded during tension because the experimental setup was not equipped with an appropriate sensor.

EBSD was utilized to study the microstructure and texture evolution of beryllium during tension. The analysis has been performed using a scanning electron microscope MIRA3 (Tescan) for the specimen working area of 900 $\times$ 330 μm (Figure 2) with the scanning step of 2 μm. For more detailed studies of deformation mechanisms and fracture initiation, the EBSD maps have also been obtained at higher resolution with a scanning step of 0.5 μm.

For EBSD analysis, the specimen was unloaded and extracted from the grips after reaching the predetermined value of elongation. Special equipment was used to avoid undesirable deformation during these manipulations. The specimen surface has been subjected to
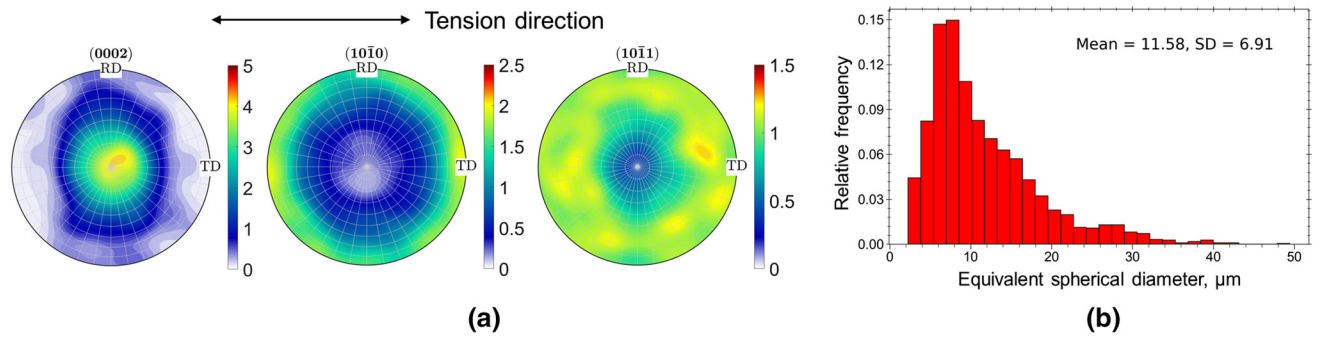
Fig. 1—The texture (*a*) and equivalent spherical diameter distribution (*b*) for 25-μm-thick beryllium foil before tension obtained using EBSD. Rolling (RD) and transverse (TD) directions correspond to cold rolling.
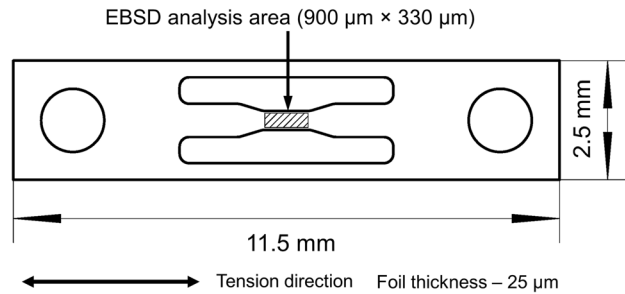

Fig. 2—Specimen configuration for tensile testing and EBSD analysis.

Table I. Measurement of Plastic Strain for Specimen Work Area

Tension Stage	Length Before Tension l_0 (μm)	Length After Tension l_1 (μm)	Logarithmic Strain (ε)
1 (initial state)	900	—	—
2	900	913	0.014
3	900	1003	0.11

plasma cleaning for 15 minutes with a gas concentration of O = 25 pct, Ar = 75 pct using a Fischione Nano-Clean model 1070 before each analysis to improve the recognition quality and eliminate the effect of «residue». HKL software was used for EBSD map processing and grain reconstruction. The modified Kuwahara filter[43] was used to reduce the noise on the obtained EBSD maps. The boundaries with misorientation angles $\omega > 15$ deg and $\omega = 2–15$ deg between adjacent grains (subgrains) were considered high-angle (HAGB) and low-angle (LAGB) boundaries, respectively.

For further analysis, the actual values of the accumulated plastic strain were calculated from the lengths of the working area before and after tension l_0 and l_1, respectively:

$$\varepsilon = \ln(l_1/l_0). \qquad [1]$$

The measurements showed (Table I) that the strain of $\varepsilon = 0.11$ had been reached in the working area before the macroscopic fracture occurred.

B. *Micromechanical Simulations of Beryllium Tension*

To determine the reasons and mechanisms of crack initiation, the distributions of the accumulated strain and stresses were estimated and the activity of SS in beryllium during tension was evaluated.

1. Crystal plasticity model

Micromechanical simulations have been performed using DAMASK software that utilizes a spectral method to solve the boundary value problem for mechanical equilibrium.[44] This approach is preferable for EBSD-based modeling compared to the traditional finite element method, which suffers from the numerical difficulties associated with significant stress and strain gradients resulting from grain interactions.[45]

A quarter of the EBSD map obtained for the undeformed specimen was used for the simulations to reduce the computational time. The area with the largest count of tensile cracks was considered. The map consisting of 418 grains was discretized with 476×164 material points using MTEX software[46] with the approach proposed by Latypov.[47] It was assumed that the deformation occurred due to the slip along the basal, prismatic, or pyramidal SS. Twinning was not considered in the simulations, since no deformation twins were revealed by EBSD.

To describe the mechanical response of the material, we used the phenomenological model proposed by Hutchinson[48] and implemented in DAMASK in a modified form.[49] According to this model, the shear rate on each slip system can be computed by the following equation:

$$\dot{\gamma}^\alpha = \dot{\gamma}_0 \left| \frac{\tau^\alpha}{\tau_0^\alpha} \right|^n \text{sgn}(\tau^\alpha), \qquad [2]$$

where $\dot{\gamma}_0$—the reference shear rate, τ—the slip resistance, n—the strain rate sensitivity of slip, and α—designation of the SS. Sgn stands for the signum function that determines the sign of the real value function: it

Table II. Crystal Plasticity Model Parameters for Beryllium at Room Temperature

Elastic Constants (GPa)				
C11	C33	C44	C12	C13
292.0	349.0	163.0	24.0	6.0

Parameters of the Phenomenological Model

Designation	$\dot{\gamma}_0$	n	a	q	h_0
Description	reference shear rate	strain rate sensitivity parameter	slip hardening parameter	latent hardening parameter	slip hardening parameter
Unit	s^{-1}	—	—	—	MPa
Value	0.001	20.0	2.25	1.0	1200.0

Hardening Parameters

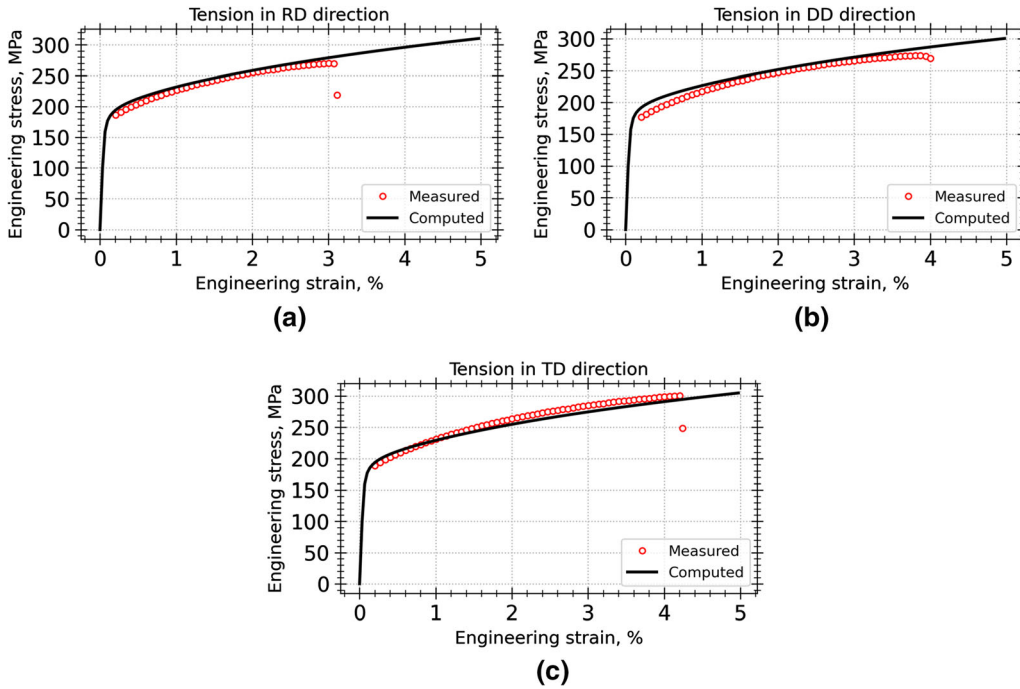| Slip system	slip resistance τ_0, MPa	saturation stress τ_∞, MPa
Basal {0001} ⟨11–20⟩	47.5	90.0
Prismatic {10–10} ⟨11–20⟩	67.5	180.0
Pyramidal {11–22} ⟨11–23⟩	320.0	2085.0

Fig. 3—Comparison between predicted and measured stress–strain curves for static tension in (*a*) rolling direction; (*b*) diagonal direction; (*c*) transverse direction. The experimental curves for beryllium foil with a thickness of 150 μm and with a basal fiber ⟨0001⟩ texture were measured in Ref. [17].

attributes + 1 for positive input values and − 1 for negative input values.

The evolution of slip resistance due to hardening can be described as

$$\dot{\tau}_0^\alpha = \sum_{\alpha'=1}^{N_s} h_{\alpha\alpha'} |\dot{\gamma}^{\alpha'}|, \qquad [3]$$

where $h_{\alpha\alpha'}$—the hardening matrix.

The hardening matrix describes the micromechanical interaction between different slip systems empirically:

$$h_{\alpha\alpha'} = q_{\alpha\alpha'} \left[h_0 \left(1 - \frac{\tau_0^\alpha}{\tau_\infty^\alpha} \right)^a \right], \qquad [4]$$
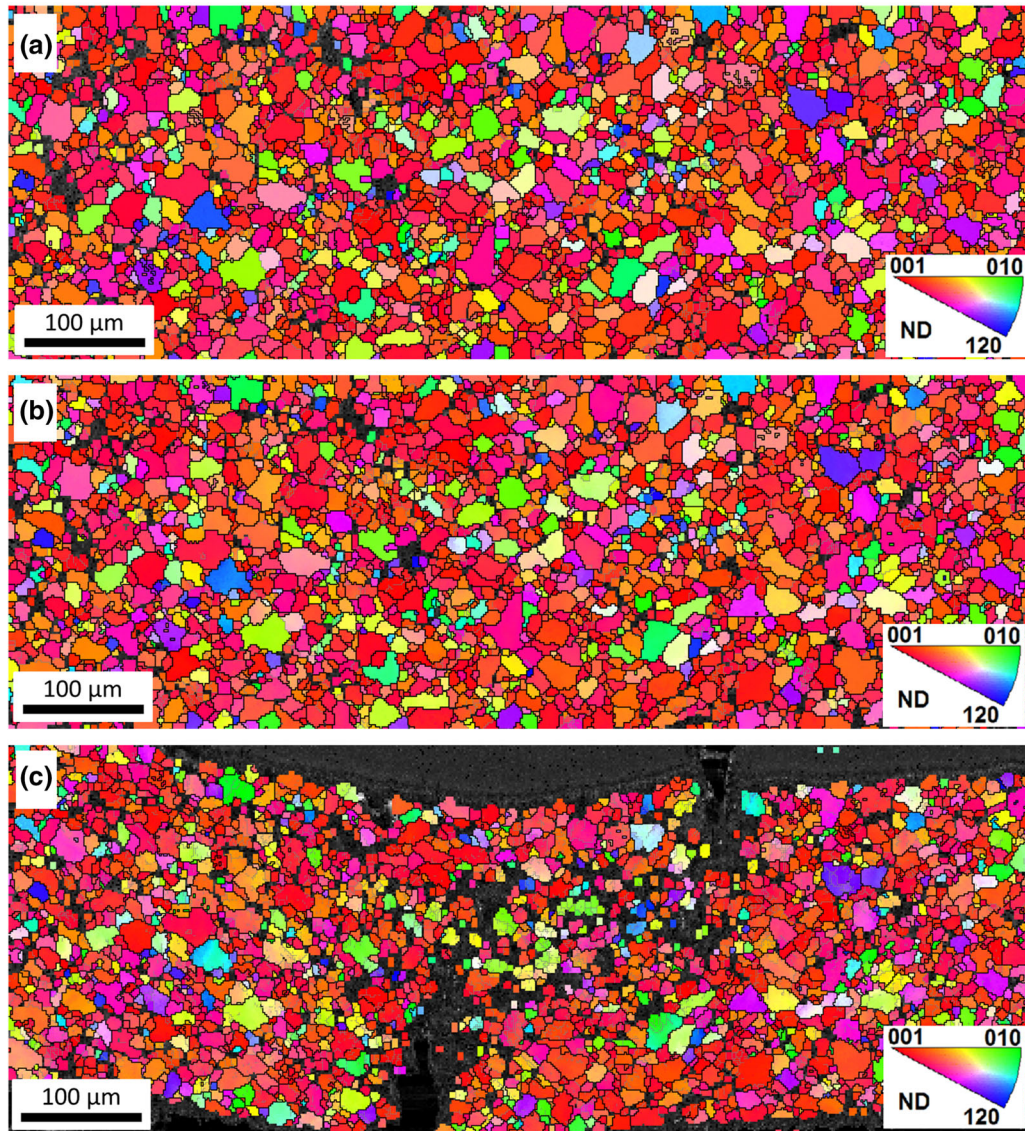
Fig. 4—EBSD maps obtained after different stages of foil tension: (*a*) initial state; (*b*) after tension up to logarithmic strain of $\varepsilon = 0.014$; (*c*) after tension up to logarithmic strain of $\varepsilon = 0.11$.

where h_0, a, and τ_∞ are slip hardening parameters, $q_{\alpha\alpha'}$—latent hardening parameter.

The contribution of slip system interactions to strain hardening has not been considered during modeling, so $q_{\alpha\alpha'}$ was chosen as 1.

It should be noted that more complex and physically sound hardening models are presented in the literature.[50–53] However, a large number of hardening parameters should be determined for their application that seems unjustified in the absence of twinning and with relatively small strains.

Comparison between the average grain size [11.6 μm, Figure 1(b)] and the sample thickness (25 μm) suggests that no more than 1–2 grains were located in the thickness direction. Therefore, the plane stress state has

been enforced by setting the following periodic boundary conditions:

$$\dot{F} = \begin{bmatrix} 1 & 0 & 0 \\ 0 & * & 0 \\ 0 & 0 & * \end{bmatrix} \,\&\, P = \begin{bmatrix} * & * & * \\ * & 0 & * \\ * & * & 0 \end{bmatrix}, \qquad [5]$$

where $\dot{F}$ is the rate of the deformation gradient tensor, P is the first Piola–Kirchhoff stress tensor.

2. Determining the hardening parameters

The accuracy of prediction of the material response during deformation directly depends on the set of hardening parameters used in Eqs. [2]–[4].[54] As a rule, the parameter fitting is performed based on the experimental data on the material behavior under different loading conditions.[12,55,56] Since the stress–strain curves
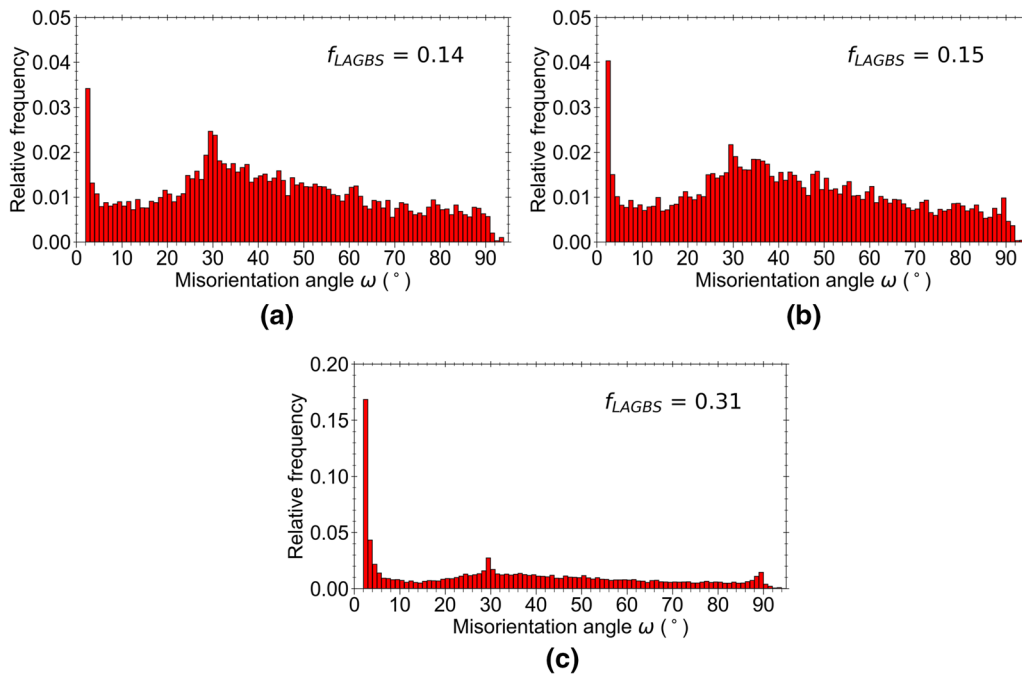
Fig. 5—Misorientation angle distribution at different stages of foil tension: (*a*) initial state; (*b*) after tension up to logarithmic strain of $\varepsilon = 0.014$; (*c*) after tension up to logarithmic strain of $\varepsilon = 0.11$.
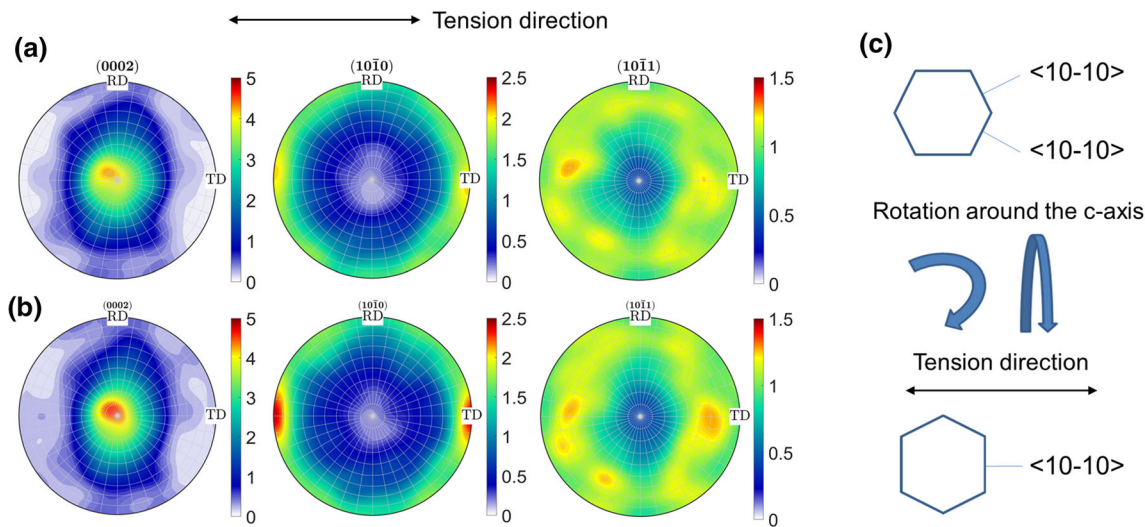

Fig. 6—The measured texture of beryllium foil after tension up to the different logarithmic strains $\varepsilon = 0.014$ (*a*) and $\varepsilon = 0.11$ (*b*) and schematic representation of beryllium texture evolution during tension (*c*). RD and TD directions correspond to cold rolling.

were not recorded in our experiments, the hardening parameters were calibrated from the tension curves obtained for the 150-μm-thick foils in our previous work.[17] To compute the stress–strain curves, a representative volume element (RVE) consisting of 512 grains was constructed according to the actual foil texture. The hardening parameters were evaluated by fitting the stress–strain curves for the foil with a basal fiber $\langle 0001 \rangle$ texture, which exhibited the highest ductility for all tension directions. The mean squared error was

minimized using a gradient-based optimization method *fmincon* implemented in Matlab. The hardening parameters obtained with the above procedure, the other parameters of the phenomenological model, and the elastic constants of beryllium (according to[57]), are presented in Table II. The calculations showed [Figures 3(a) through (c)] that the fitted set of parameters provided a good agreement between the predicted and experimental stress–strain curves.
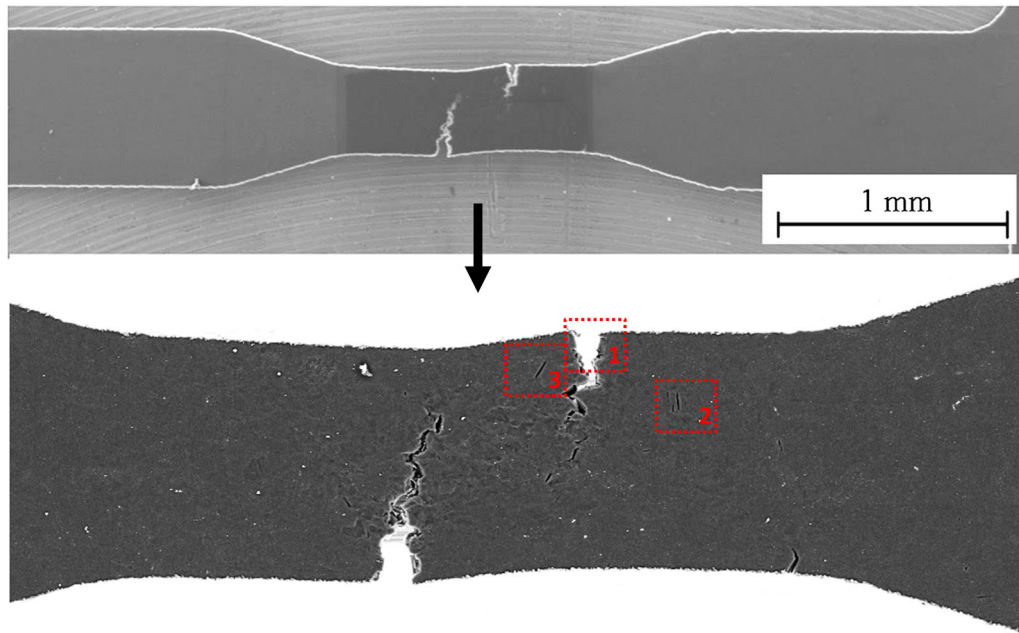
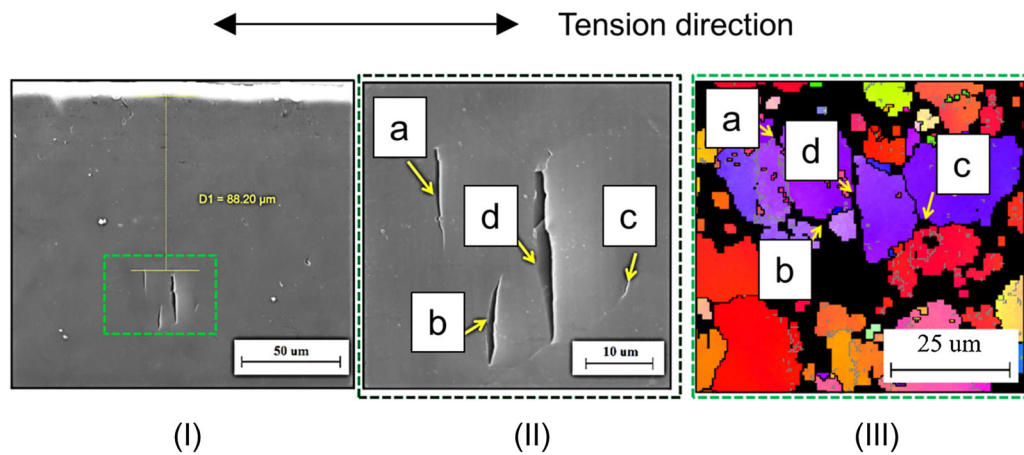Fig. 7—SEM images of the specimen working area after macroscopic fracture.

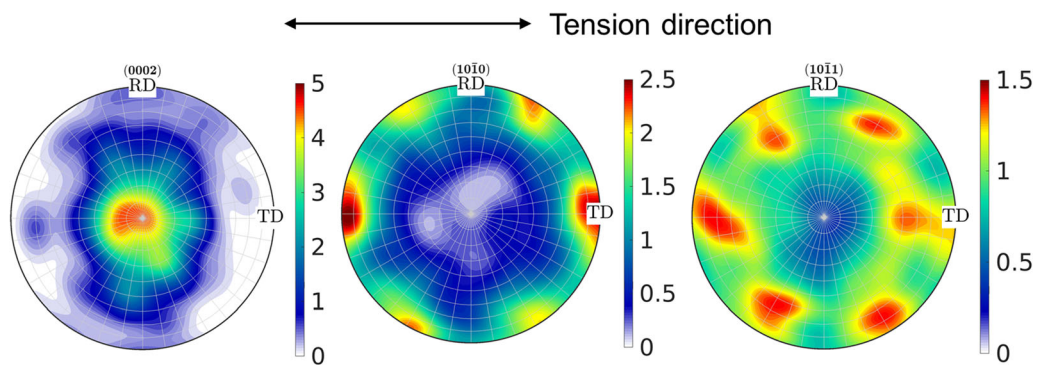Fig. 8—SEM images (I and II) and EBSD map (III) of the cracking area.

Fig. 9—Texture of beryllium foil after tension up to logarithmic strain of $\varepsilon = 0.11$ predicted by simulation (RD and TD directions correspond to cold rolling).
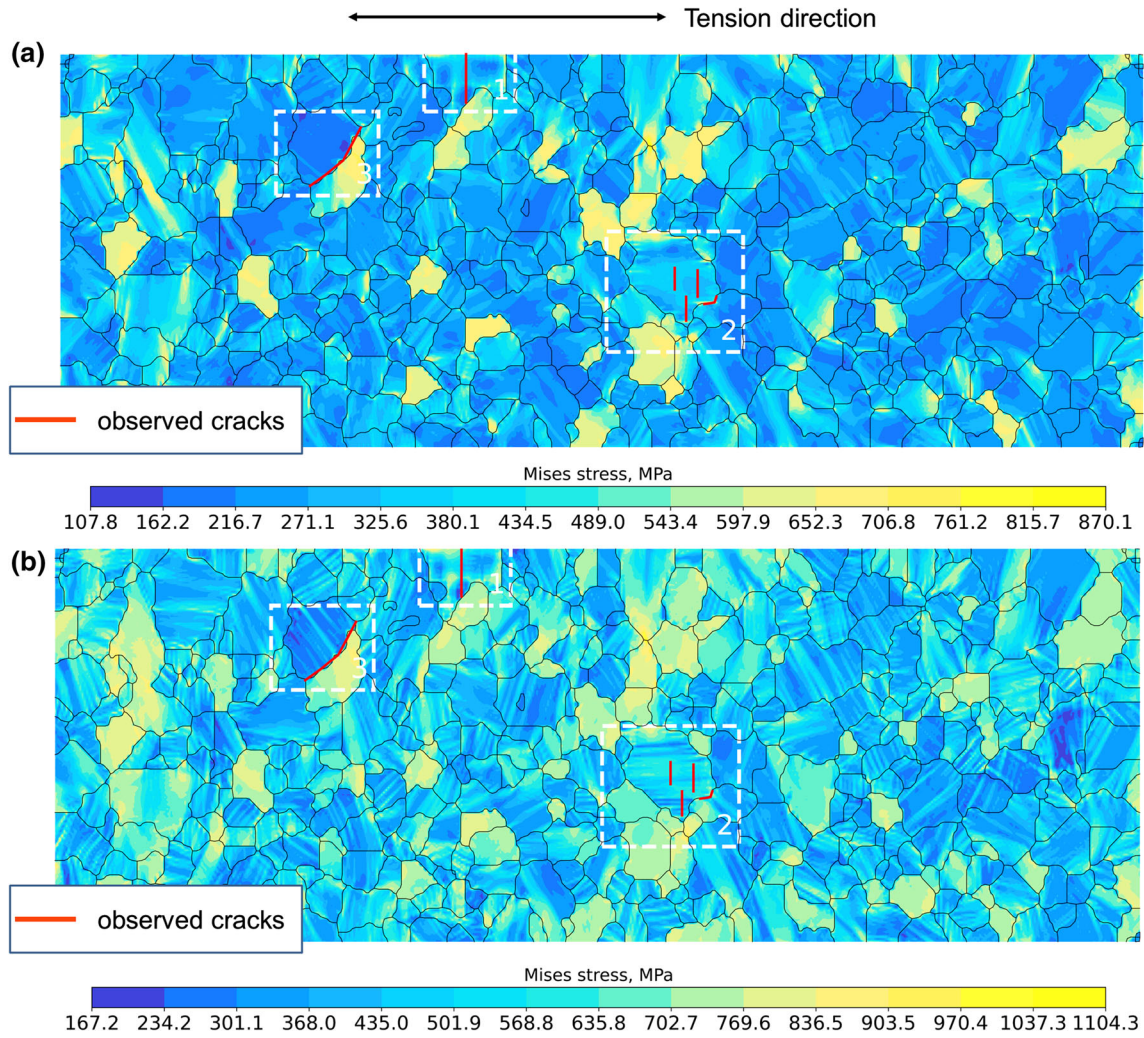
Fig. 10—Computed values of Mises stress in specimen after tension up to logarithmic strain of (a) $\varepsilon = 0.014$; (b) $\varepsilon = 0.11$.

3. Estimation of fracture probability

To assess the failure probability, we used the modified Cockcroft–Latham failure criterion (CL) [58]:

$$C = \int_0^{\bar{\varepsilon}} \frac{\sigma_1}{\bar{\sigma}} \, d\bar{\varepsilon}, \qquad [6]$$

where σ_1 is the maximum principal stress, $\bar{\sigma}$ is the effective stress, and $\bar{\varepsilon}$ is the effective strain.

According to the CL criterion, fracture of material occurs when the actual value of C exceeds a certain limit that depends on the material properties. Despite its relative simplicity, the criterion reliably predicts the locations of crack initiation and has an acceptable accuracy; therefore it is often used to predict fracture and evaluate workability in metalworking processes.[59–64]

Another important parameter for fracture probability estimation is the stress triaxiality (ST):

$$\eta = \frac{\sigma_m}{\bar{\sigma}}, \qquad [7]$$

where σ_m is the mean normal stress.

Values of mean normal stress can be computed as

$$\sigma_m = \frac{\sigma_1 + \sigma_2 + \sigma_3}{3}, \qquad [8]$$

where σ_1, σ_2, and σ_3 are principal stresses.

It is well known that stress triaxiality affects strongly the value of fracture strain (i.e., the strain that can be accommodated by a material before a fracture occurs).[65] Experiments showed that fracture strain decreased with increasing ST.[66–68]

III. RESULTS AND DISCUSSION

A. Evolution of the Structure and Texture of Beryllium Foil Subjected to Static Tension

Figures 4(a) through (c) show the EBSD maps of the specimen work area at different stages of tension up to the macroscopic fracture.

It can be seen that strain accumulation triggers the process of LAGB formation [light lines in Figure 4(c)]. To quantify the proportion between LAGB and HAGB,
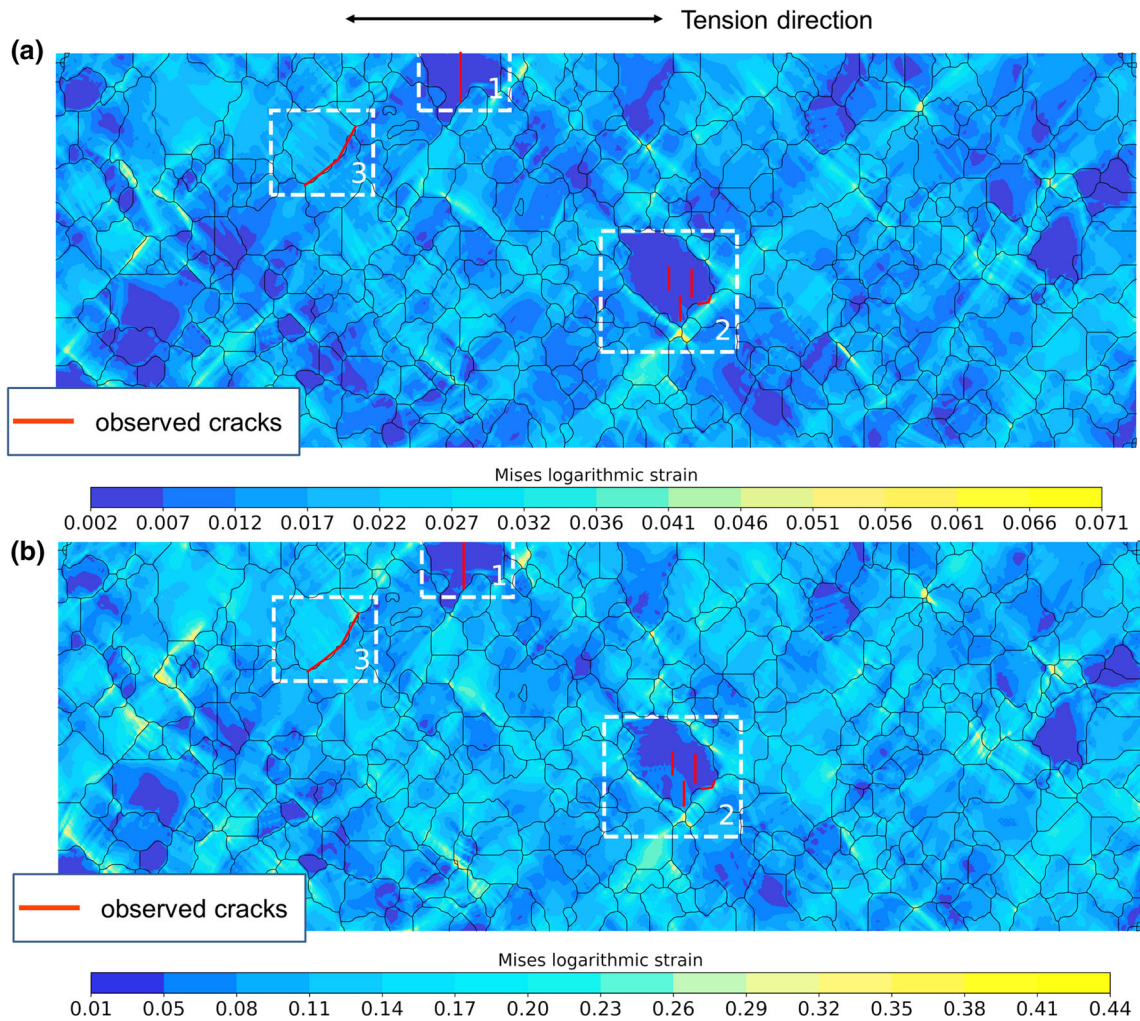
misorientation angle distributions were plotted (Figure 5). It can be seen [Figure 5(a)] that the undeformed state of beryllium before tension is characterized by an almost completely recrystallized structure with a volume fraction of LAGB of no more than 0.14. Small deformations of $\varepsilon = 0.014$ [Figure 5(b)] had practically no effect on the quantitative change in the ratio between LAGB and HAGB (the ratio of LAGB $f = 0.15$). After strain accumulation up to $\varepsilon = 0.11$, the fraction of LAGB was $f = 0.31$ [Figure 5(c)]. It should be noted that the formation of new boundaries is extremely inhomogeneous. According to Figure 4(c), the process of LAGB formation in some grains was faster than in the surrounding grains. This effect can be associated with the inhomogeneity of the strain distribution in the specimen.

The reconstructed pole figures [Figures 6(a) and (b)] showed that the initial ⟨0001⟩ fiber texture of beryllium was transformed into the {0001} ⟨10–10⟩ texture after tension. The presence of the maxima in the ⟨10–10⟩ directions along the tension direction indicates that crystallite rotation occurs not only in the foil plane but also in the plane perpendicular to the tension direction [Figure 6(c)].

B. *Fracture of Beryllium Foil Under Static Tension*

Figure 7 shows SEM images of the specimen working area after a macroscopic fracture.

It can be seen that the macroscopic cracks (zone 1 in Figure 7) coexist with the relatively small cracks that grow in a perpendicular direction (zone 2 in Figure 7) and at an angle (zone 3 in Figure 7) to the tension direction. For more detailed studies, an additional EBSD map was captured in the cracking region (zone 2 in Figure 7) with a scanning step reduced to 0.5 μm (see Figure 8 and Supplementary Figure S-1). Determination of the crack positions by comparison of EBSD maps and SEM images is provided in more detail in the electronic supplementary data file. Results showed that both transgranular (cracks a, b, and d in Figure 8) and intergranular (crack c in Figure 8) cracks were formed in the region.
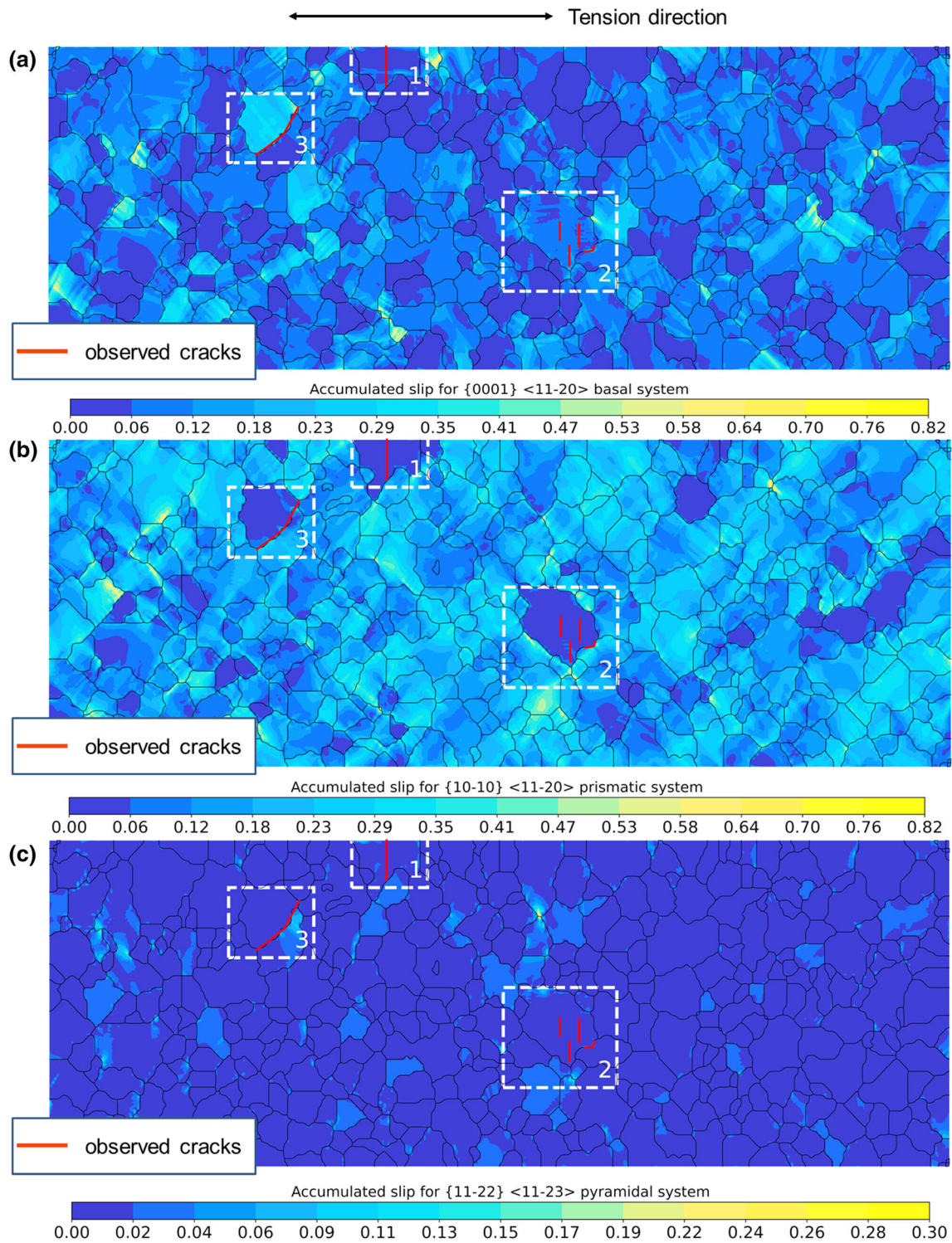
(a)

observed cracks

Accumulated slip for {0001} <11-20> basal system

| 0.00 | 0.06 | 0.12 | 0.18 | 0.23 | 0.29 | 0.35 | 0.41 | 0.47 | 0.53 | 0.58 | 0.64 | 0.70 | 0.76 | 0.82 |

(b)

observed cracks

Accumulated slip for {10-10} <11-20> prismatic system

| 0.00 | 0.06 | 0.12 | 0.18 | 0.23 | 0.29 | 0.35 | 0.41 | 0.47 | 0.53 | 0.58 | 0.64 | 0.70 | 0.76 | 0.82 |

(c)

observed cracks

Accumulated slip for {11-22} <11-23> pyramidal system

| 0.00 | 0.02 | 0.04 | 0.06 | 0.09 | 0.11 | 0.13 | 0.15 | 0.17 | 0.19 | 0.22 | 0.24 | 0.26 | 0.28 | 0.30 |

Fig. 12—Computed values of accumulated slip along different SS in specimen after tension up to logarithmic strain of $\varepsilon = 0.11$: a) basal {0001} ⟨11–20⟩; (b) prismatic {10–10} ⟨11- 20⟩; (c) pyramidal {11–22} ⟨11–23⟩.

C. Results of Crystal Plasticity Simulations

Figure 9 shows the reconstructed pole figures characterizing the foil texture after tension up to $\varepsilon = 0.11$ (stage 3, Table 1). A good agreement between the predicted and measured textures [Figure 6(b)] confirms

reliability of the simulations and accuracy of the used hardening parameters.

The calculated distributions of the Mises stress and the accumulated logarithmic strain for different tension stages are shown in Figures 10 and 11. It can be seen that the stress localization is already observed at the
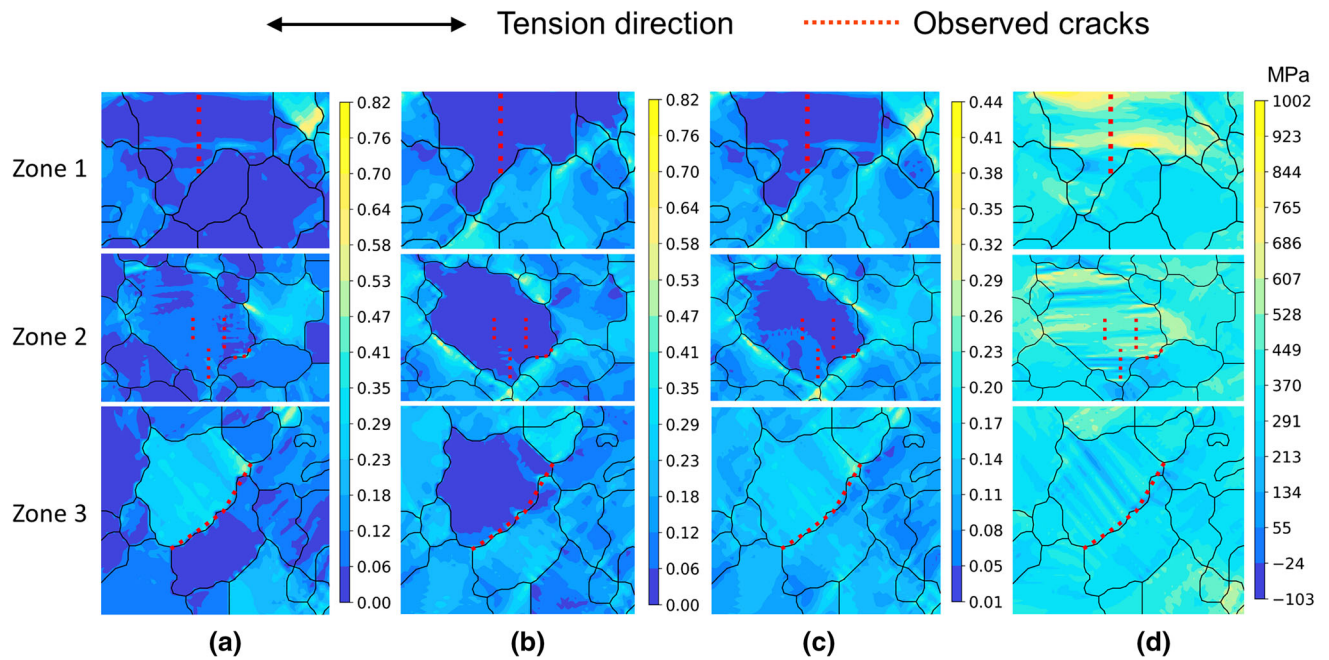
Fig. 13—The values of accumulated slip for basal (*a*) and prismatic (*b*) slip systems, Mises logarithmic strain (*c*) and the stress component along the tension direction σ_{11} (*d*) for fracture zones 1–3.
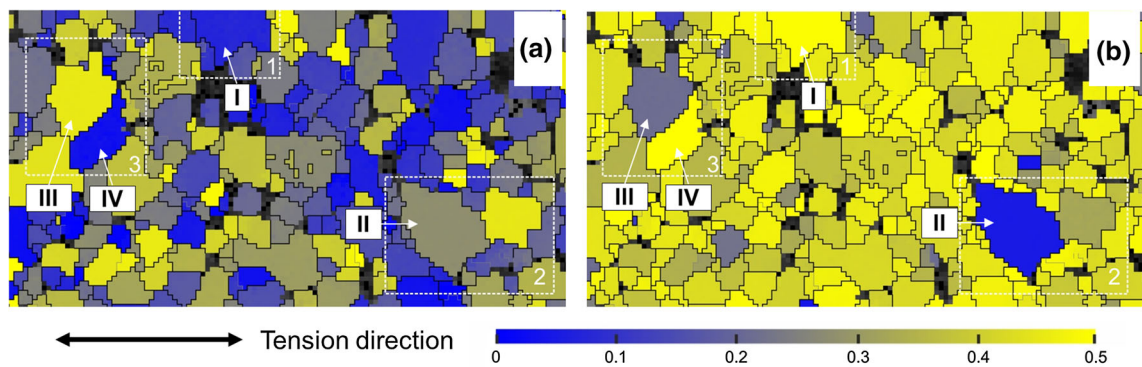

Fig. 14—Schmid factor maps for basal (*a*) and prismatic (*b*) slip systems for the undeformed state in tension direction.

initial tension stage [Figure 10(a)]. As far as strain accumulates in certain grains and the slip resistance increases due to hardening, other grains begin to deform, and the stress distribution becomes more uniform [Figure 10(b)].

A significant stress gradient leads to an extremely inhomogeneous distribution of accumulated plastic strain (Figure 11). At the initial tension stages, when the macroscopic strain of the specimen is only $\varepsilon = 0.014$, strain can reach the values of $\varepsilon = 0.07$ in some regions which is 5 times higher [Figure 11(a)].

The strain inhomogeneity becomes less pronounced with further tension: the value of the accumulated strain becomes ∼ 0.4–0.44 when the average macroscopic strain measured by the elongation of the working area is $\varepsilon = 0.11$ [Figure 11(b)]. At the same time, there are some grains in which the accumulated strain is almost zero (regions 1 and 2 in Figure 11). It should be noted

that the highest values of the accumulated strain are typically observed at grain boundaries, especially at triple junctions.

The heterogeneity of strain distribution can be explained by different activities of slip systems in the grains under tension. Figures 12(a) through (c) show the distributions of accumulated slip for different SS after tension up to $\varepsilon = 0.11$.

It can be seen that the prismatic slip is the main deformation mechanism in the considered case, while the slip along the basal SS is restricted in most grains. Sliding along the pyramidal SS is activated in some grains due to the exhaustion of the slip possibility along the other slip systems. Such a mechanism is not typical of the beryllium deformation at room temperature, where the basal slip normally dominates.[15] The observed activity of the slip systems can be explained by the formation of a ⟨0001⟩ fiber texture.
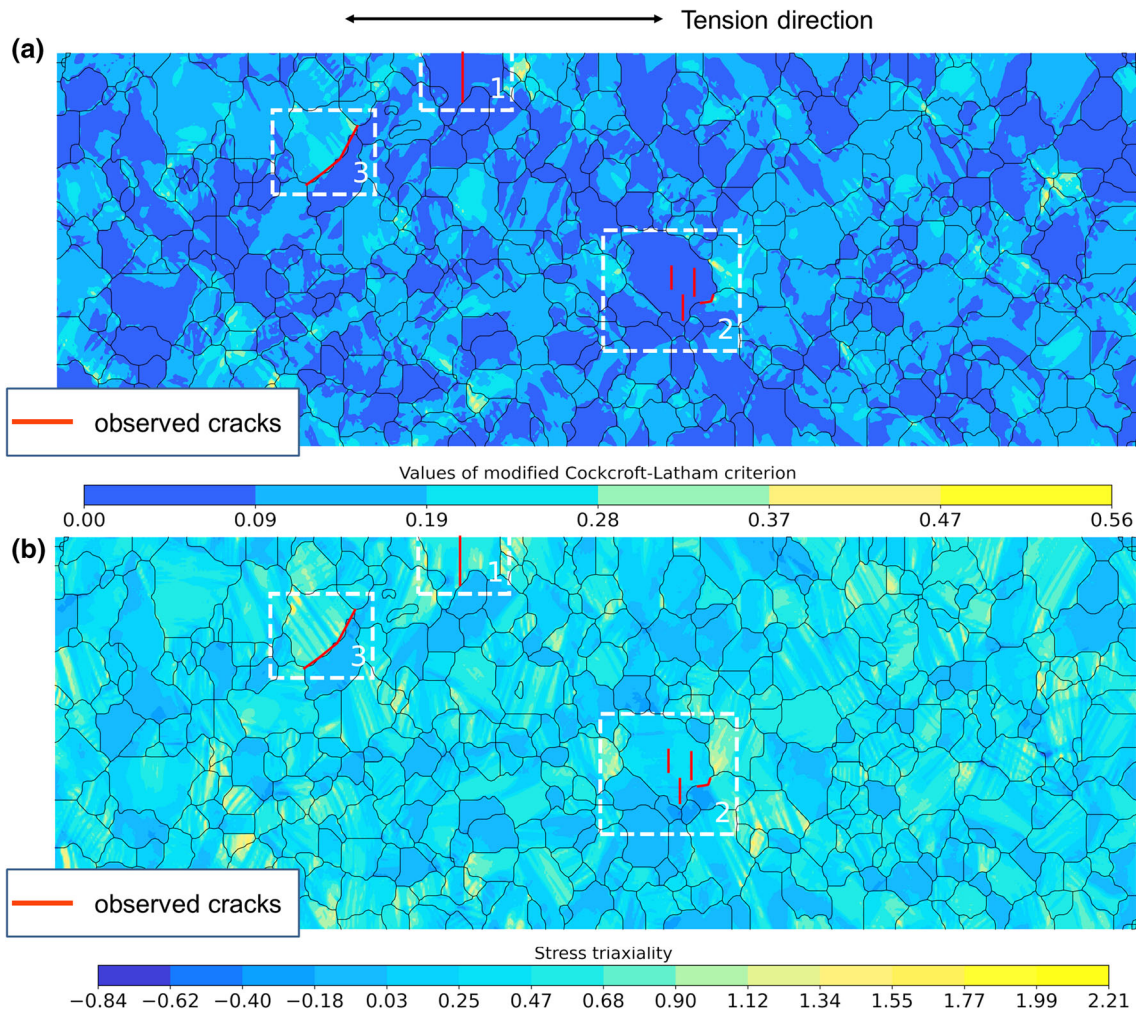
Fig. 15—Computed values of the modified Cockcroft–Latham criterion (a) and stress triaxiality parameter (b) in the specimen after tension up to logarithmic strain of ε = 0.11.

D. Analysis of the Beryllium Fracture Mechanism

Analysis of the accumulated slip for the basal and prismatic SS in fracture zones 1–3 [Figures 13(a) and (b)] showed that the formation of cracks is associated with blocking of the prismatic slip in all considered cases. In addition, the possibility of basal slip activation and the orientation of neighboring grains also have a significant effect on the fracture mechanism. When both basal and prismatic slip are simultaneously blocked in the grain (zones 1, 2 in Figure 13), a transgranular fracture is observed. It is associated with the appearance of significant tensile stresses in the tension direction σ_{11} [Figure 13(d)] and with the formation of cracks located perpendicular to the same direction. Since the values of accumulated strain are only $\varepsilon \sim 0.02$–0.04 [Figure 13(c)] this can be characterized as a brittle fracture. Consequently, the grain in this case can be considered as a brittle nondeformable inclusion.

If prismatic slip is blocked in the grain, but there is a possibility of basal slip activation, the observed crack is located along the grain boundary (zone 3 in Figure 13). The formation of intergranular crack is accompanied by

the accumulation of significant strains up to the values of ~ 0.3–0.35. Therefore, it can be assumed that its appearance is associated with the fracture caused by plasticity exhaustion. Thus, the regions of crack initiation should be well captured by the ductile damage criteria in this case. A comparison of the logarithmic strains with the values of accumulated slip shows that the strain localization occurs at the boundary of those adjacent grains which have favorable and unfavorable conditions for prismatic slip, respectively, i.e., when a significant gradient of prismatic slip activity exists (zone 3 in Figure 13). Such localization pattern is typical of hcp metals. For example, a significant stress concentration was found at the boundary between the regions with the so-called "hard" and "soft" orientations in the Ti–6Al–4V alloy.[69]

Analysis of the calculated values of the Schmid factor showed (Figure 14) that some grains had favorable orientations for prismatic [grain I in zone 1, Figure 14(b)] or for basal slip [grain II in zone 2, Figure 14(a)]. However, both basal and prismatic slips were blocked in these grains during tension, which caused the formation of cracks and brittle fracture. On

the contrary, for other grains [grains III and IV in zone 3, Figure 14], the values of the accumulated slip were fully consistent with the Schmid factor for both the basal $\{0001\}$ $\langle 11\text{–}20 \rangle$ and the prismatic $\{10\text{–}10\}$ $\langle 11\text{–}20 \rangle$ SS. Thus, the assumption about the effect of stress localization on the possibility of slip activation is also confirmed for beryllium. Since the fracture mechanism is closely related to the activity of SS, the role of grain interactions in the deformation of polycrystalline beryllium seems to be significant.

The calculated values of the CL criterion are shown in Figure 15(a).

It can be seen that the values (0.37–0.47) are significantly higher in the cracking region 3 than in most of the other grain areas, owing to strain localization. Thus, the CL criterion reliably predicts the regions where the intergranular cracks may form. It should be noted that the CL criterion cannot capture the transgranular cracking in the zones 1–2, because of the minimal values of the accumulated strain in the fractured grains. Analysis of the stress triaxiality distribution [Figure 15(b)] also shows that an unfavorable stress state is observed in the cracking regions, as evidenced by the high values of $\eta \sim 1.3\text{–}2$. Nevertheless, there are certain regions in the specimen with the large values of CL criterion and ST, but fracture does not occur in those areas. Thus, we can conclude that the values of fracture strain and the critical value of the CL criterion strongly depend on the grain orientation.

IV. CONCLUSIONS

In this work, the mechanisms of deformation and crack initiation in polycrystalline beryllium during static tension were investigated using EBSD analysis and micromechanical simulations. The experiments and calculations showed that the fracture of beryllium was closely related to its crystallographic texture. The main conclusions can be formulated as follows:

(1) Cold deformation of beryllium under tension is characterized by a significant inhomogeneity in the stress and strain distribution. Depending on the grain orientation, the accumulated strain may either be much higher than the average strain of the specimen, or be almost zero.

(2) The fracture of beryllium during cold tension has a complex character and occurs by two mechanisms. Brittle transgranular fracture takes place at small strains of $\varepsilon \sim 0.02\text{–}0.04$ through the grains in which slip along the basal and prismatic slip system is blocked. At the same time, activation of the prismatic slip prevents the fracture at the accumulated strains of up to $\varepsilon \sim 0.3\text{–}0.35$, which are significant for the beryllium at the temperatures of cold deformation. Localization of plastic strain at the conjugation of grains with favorable and unfavorable conditions for a prismatic slip leads to the formation of intergranular cracks due to the beryllium plasticity exhaustion.

(3) The possibility of basal or prismatic slip activation during static tension is affected not only by grain orientation but also by the stress gradient. Thus, the accounting of grain interactions is critically important for the analysis of polycrystalline beryllium fracture.

(4) The ductile fracture of beryllium can be adequately predicted using the modified Cockcroft–Latham criterion or the stress triaxiality parameter. Meanwhile, the fracture strain and the limiting value of the modified Cockcroft–Latham criterion strongly depend on the grain orientation.

CONFLICT OF INTEREST

The authors declare that they have no conflict of interest.

DATA AVAILABILITY

The data that support the findings of this study are available from the corresponding author upon reasonable request.

SUPPLEMENTARY INFORMATION

The online version contains supplementary material available at https://doi.org/10.1007/s11661-023-07090-0.

REFERENCES

1. T. Parsonage: *Mater. Sci. Technol.*, 2000, vol. 16, pp. 732–38.
2. W.J. Haws: *JOM*, 2000, vol. 52, pp. 35–37.
3. Y. Wang, C. Wang, Z. Meng, Y. Liu, J. Liu, Y. Li, and L. Yang: *Nucl. Mater. Energy*, 2022, vol. 31, 101181.
4. V. Kuksenko, K. Ammigan, B. Hartsell, C. Densham, P. Hurh, and S. Roberts: *J. Nucl. Mater.*, 2017, vol. 490, pp. 260–71.
5. V. Kuksenko, A. Lunev, E. Darnbrough, C. Densham, P. Hurh, and S. Roberts: *J. Nucl. Mater.*, 2021, vol. 555, 153130.
6. N. Zimber and P. Vladimirov: *J. Nucl. Mater.*, 2022, vol. 568, 153855.
7. T.B. Parsonage: E. Atad-Ettedgui and P. Dierickx, eds., 2004, p. 39.
8. M.J. Russo, S. LoBiondo, B. Coon, M. Engelhardt, W. Pinzon, W.A. Goodman and J.L. Robichaud, eds., 2007, p. 66660T.
9. H.R. Beguiristain, J.T. Cremer, M.A. Piestrup, C.K. Gary, and R.H. Pantell: *Opt. Lett.*, 2002, vol. 27, p. 778.

10. O.V. Yurkevich, K.Y. Maksimova, A.Y. Goikhman, A.A. Snigirev, and I.I. Snigireva: *J. Surf Investig. X-ray Synchrotron Neutron Tech.*, 2015, vol. 9, pp. 243–47.
11. Z. Chen, G. Jin, K. Chen, Y. Chen, Y. Song, L. Hu, L. Niu, X. Sheng, Y. Cheng, and K. Lu: *Fusion Eng. Des.*, 2013, vol. 88, pp. 3280–286.
12. D.W. Brown, S.P. Abeln, W.R. Blumenthal, M.A.M. Bourke, M.C. Mataya, and C.N. Tomé: *Metall. Mater. Trans. A*, 2005, vol. 36, pp. 929–39.
13. M. Knezevic, I.J. Beyerlein, D. Brown, T.A. Sisneros, and C. Tomé: *Int. J. Plast.*, 2013, vol. 49, pp. 185–98.
14. I.A. Shishov, V.V. Mishin, and I.A. Kasatkin: *Mater. Charact.*, 2021, vol. 180, 111427.
15. V.V. Mishin, I.A. Shishov, O.N. Stolyarov, I.A. Kasatkin, and P.A. Glukhov: *Mater. Charact.*, 2020, vol. 164, 110350.
16. V. Kuksenko, S. Roberts, and E. Tarleton: *Int. J. Plast.*, 2019, vol. 116, pp. 62–80.
17. V.V. Mishin, I.A. Shishov, O.N. Stolyarov, I.A. Kasatkin, and P.A. Glukhov: *Materialia*, 2020, vol. 11, 100726.
18. J. Beuers, S. Jönsson, and G. Petzow: *Acta Metall.*, 1987, vol. 35, pp. 2277–287.
19. A. Couret and D. Caillard: *Philos. Mag. A*, 1989, vol. 59, pp. 783–800.
20. V.C. Kannan and S. Weissmann: *J. Appl. Phys.*, 1971, vol. 42, pp. 2632–638.
21. F. Aldinger: in *Beryllium Science and Technology, Volume 1*, D. Webster, ed., Plenum Press, New York, 1979.
22. D. Webster, ed.: *Beryllium Science and Technology*, Springer, Boston, 1979.
23. A. Staroselsky and L. Anand: *Int. J. Plast.*, 2003, vol. 19, pp. 1843–864.
24. W. Li, L. Wang, B. Zhou, C. Liu, and X. Zeng: *J. Mater. Sci. Technol.*, 2019, vol. 35, pp. 2200–206.
25. D.W. Brown, M.A.M. Bourke, C.N. Tomé, R. Varma, T.M. Holden, and B. Clausen: *Metall. Mater. Trans. A*, 2003, vol. 34, pp. 1439–449.
26. D.W. Brown, I.J. Beyerlein, T.A. Sisneros, B. Clausen, and C.N. Tomé: *Int. J. Plast.*, 2012, vol. 29, pp. 120–35.
27. N.C. Ferreri, Z. Feng, D.J. Savage, D.W. Brown, B. Clausen, T.A. Sisneros, and M. Knezevic: *Int. J. Plast.*, 2022, vol. 150, 103217.
28. T.A. Book and M.D. Sangid: *Mater. Charact.*, 2016, vol. 122, pp. 104–12.
29. K. Il-Kim, Y. Oh, D.U. Kim, J.-H. Kang, N.I. Cho, K.H. Oh, J.-Y. Kang, and H.N. Han: *Met. Mater. Int.*, 2022, vol. 28, pp. 1094–104.
30. N. Saeidi, M. Jafari, F. Ashrafizadeh, M. Karimi, S. Ziaei-Rad, and H.S. Kim: *Mater. Res. Express*, 2018, vol. 5, 126507.
31. R. Jiang, W. Zhang, L. Zhang, Y. Zhao, L. Zhang, and Y. Song: *Fatigue Fract. Eng. Mater. Struct.*, 2022, vol. 45, pp. 1635–651.
32. S. Gelles, V. Nerses, and J.M. Siergiej: *JOM*, 1963, vol. 15, pp. 843–48.
33. G. Sumner: *Int. J. Fract. Mech.*, 1966, vol. 2, pp. 448–59.
34. M. Diehl, M. Wicke, P. Shanthraj, F. Roters, A. Brueckner-Foit, and D. Raabe: *JOM*, 2017, vol. 69, pp. 872–78.
35. W.F. Spurr and W.E. Quist: in *1973 International Automotive Engineering Congress and Exposition*, SAE International, 1973.
36. M.K. Samal, A. Syed, J. Chattopadhyay, A.M. Ram, B. Paul, and M.C. Reddy: *J. Nucl. Mater.*, 2020, vol. 535, 152189.
37. V. Grigoriev and S. Andersson: *Influence of Texture on Fracture Toughness of Zircaloy Cladding*, Sweden, 1997.
38. G.C. Prakash, H.N. Bar, S. Sivaprasad, S. Tarafder, and S. Biswas: *IOP Conf. Ser. Mater. Sci. Eng.*, 2021, vol. 1121, 012028.
39. M.A. Beltran-Zuñiga, J.L. González-Velázquez, D.I. Rivas-López, H.J. Dorantes-Rosales, and F. Hernández-Santiago: *Fatigue Fract. Eng. Mater. Struct.*, 2018, vol. 41, pp. 749–61.
40. G. Lagerberg: *Metallurgical Viewpoints on the Brittleness of Beryllium*, Sweden, 1960.
41. R. Armstrong: *Acta Metall.*, 1968, vol. 16, pp. 347–55.
42. J. Wittenauer, T.G. Nieh, and G. Waychunas: *J. Mater. Sci.*, 1992, vol. 27, pp. 2653–659.
43. F.J. Humphreys, P.S. Bate, and P.J. Hurley: *J. Microsc.*, 2001, vol. 201, pp. 50–8.
44. F. Roters, M. Diehl, P. Shanthraj, P. Eisenlohr, C. Reuber, S.L. Wong, T. Maiti, A. Ebrahimi, T. Hochrainer, H.-O. Fabritius, S. Nikolov, M. Friák, N. Fujita, N. Grilli, K.G.F. Janssens, N. Jia, P.J.J. Kok, D. Ma, F. Meier, E. Werner, M. Stricker, D. Weygand, and D. Raabe: *Comput. Mater. Sci.*, 2019, vol. 158, pp. 420–78.
45. P. Eisenlohr, M. Diehl, R.A. Lebensohn, and F. Roters: *Int. J. Plast.*, 2013, vol. 46, pp. 37–53.
46. R. Hielscher and H. Schaeben: *J. Appl. Crystallogr.*, 2008, vol. 41, pp. 1024–37.
47. M.I. Latypov, S. Shin, B.C. De Cooman, and H.S. Kim: *Acta Mater.*, 2016, vol. 108, pp. 219–28.
48. J.W. Hutchinson: *Proc. R. Soc. London. A*, 1976, vol. 348, pp. 101–27.
49. F. Roters, P. Eisenlohr, L. Hantcherli, D.D. Tjahjanto, T.R. Bieler, and D. Raabe: *Acta Mater.*, 2010, vol. 58, pp. 1152–211.
50. B.L. Hansen, I.J. Beyerlein, C.A. Bronkhorst, E.K. Cerreta, and D. Dennis-Koller: *Int. J. Plast.*, 2013, vol. 44, pp. 129–46.
51. M. Lindroos, G. Cailletaud, A. Laukkanen, and V.-T. Kuokkala: *Mater. Sci. Eng. A*, 2018, vol. 720, pp. 145–59.
52. C.Y. Sun, N. Guo, M.W. Fu, and S.W. Wang: *Int. J. Plast.*, 2016, vol. 76, pp. 186–212.
53. S.L. Wong, M. Madivala, U. Prahl, F. Roters, and D. Raabe: *Acta Mater.*, 2016, vol. 118, pp. 140–51.
54. K. Sedighiani, M. Diehl, K. Traka, F. Roters, J. Sietsma, and D. Raabe: *Int. J. Plast.*, 2020, vol. 134, 102779.
55. S. Deng, H. Song, H. Liu, and S.-H. Zhang: *Int. J. Solids Struct.*, 2021, vol. 213, pp. 63–76.
56. A.K. Singh, L. Kaushik, J. Singh, H. Das, M. Mondal, S.-T. Hong, and S.-H. Choi: *Int. J. Plast.*, 2022, vol. 150, 103184.
57. D. Tromans: *Int. J. Res. Rev. Appl. Sci.*.
58. S.I. Oh, C.C. Chen, and S. Kobayashi: *J. Eng. Ind.*, 1979, vol. 101, pp. 36–44.
59. W. Jia, L. Wang, L. Ma, H. Li, H. Xie, and Y. Yuan: *J. Mater. Res. Technol.*, 2022, vol. 17, pp. 2047–058.
60. S. Choudhary, P.K. Singh, S. Khare, K. Kumar, P. Mahajan, and R.K. Verma: *Int. J. Impact Eng.*, 2020, vol. 140, 103557.
61. S. Stebunov, A. Vlasov, and N. Biba: *Procedia Manuf.*, 2018, vol. 15, pp. 519–26.
62. R. Zhao, X.J. Li, M. Wan, J.Q. Han, B. Meng, and Z.Y. Cai: *Mater. Des.*, 2017, vol. 130, pp. 413–25.
63. N. Hatanaka, K. Yamaguchi, and N. Takakura: *J. Mater. Process. Technol.*, 2003, vol. 139, pp. 64–70.
64. H. Talebi-Ghadikolaee, H.M. Naeini, M.J. Mirnia, M.A. Mirzai, H. Gorji, and S. Alexandrov: *Thin-Walled Struct.*, 2020, vol. 148, 106566.
65. G. Mirone: *Eng. Fract. Mech.*, 2007, vol. 74, pp. 1203–221.
66. J.-M. Seo, H.-T. Kim, Y.-J. Kim, H. Yamada, T. Kumagai, H. Tokunaga, and N. Miura: *Nucl. Eng. Technol.*, 2003, https://doi.org/10.1016/j.net.2022.02.002.
67. H. Zhang, X. Li, T. Gao, H. Song, and G. Huang: *Eng. Fract. Mech.*, 2021, vol. 258, 108127.
68. Y.C. Lin, X.-H. Zhu, W.-Y. Dong, H. Yang, Y.-W. Xiao, and N. Kotkunde: *J. Alloys Compd.*, 2020, vol. 832, 154988.
69. W. Liu, J. Huang, J. Liu, X. Wu, K. Zhang, and A. Huang: *Int. J. Fatigue*, 2021, vol. 148, 106203.